Revealing Fracture Planes with a High-Resolution Catalog of Induced Microearthquakes

Chengping Chai[1,*], Monica Maceira[1,2], Hector J. Santos-Villalobos[1], Singanallur V. Venkatakrishnan[1], Martin Schoenball[3], Pengcheng Fu[4], Clifford Thurber[5], Paul C. Schwering[6], Timothy C. Johnson[7], Hunter A. Knox[7], and EGS Collab Team[†]

[1]Oak Ridge National Laboratory, Oak Ridge, Tennessee 37830, USA

[2]Department of Physics and Astronomy, The University of Tennessee, Knoxville, Tennessee 37996, USA

[3]Lawrence Berkeley National Laboratory, Berkeley, California 94720, USA

[4]Lawrence Livermore National Laboratory, Livermore, California 94550, USA

[5]Department of Geoscience, University of Wisconsin-Madison, Madison, Wisconsin 53706, USA

[6]Sandia National Laboratories, Albuquerque, New Mexico 87185, USA

[7]Pacific Northwest National Laboratory, Richland, Washington 99352, USA

[*]Corresponding author, chaic@ornl.gov, PO Box 2008, MS6075, Oak Ridge, TN 37831

[†]Members of the EGS Collab Team are listed in Appendix A.

This manuscript has been authored in part by UT-Battelle, LLC, under contract DE-AC05-00OR22725 with the US Department of Energy (DOE). The US government retains and the publisher, by accepting the article for publication, acknowledges that the US government retains a nonexclusive, paid-up, irrevocable, worldwide license to publish or reproduce the published form of this manuscript, or allow others to do so, for US government purposes. DOE will provide public access to these results of federally sponsored research in accordance with the DOE Public Access Plan (http://energy.gov/downloads/doe-public-access-plan).

KEY POINTS

- We performed double-difference tomography at meter scale for an enhanced geothermal system
- We compared tomography results with seismic event locations fixed and inverted
- Updated seismic event locations show sharper fracture patterns than the original locations

ABSTRACT

Seismic sensors and seismic imaging have been widely used to monitor the geophysical properties of the subsurface. As subsurface engineering techniques advance, more precise monitoring systems are required. Seismic event catalogs and seismic velocity structures are two of the major outputs of seismic monitoring systems. Although seismic event catalogs and velocity structure are often studied separately, published reports suggest constraining them simultaneously can lead to better results. We conducted a double-difference seismic tomography analysis to constrain both the seismic event locations and the 3D seismic velocity structure. Passive seismic data collected from a geothermal research project in Lead, South Dakota were used to image a 3D volume on the scale of tens of meters. Specifically, around 18,500 P-wave and 8,900 S-wave arrival times from 1,874 seismic events were used. Checkerboard tests showed that the observed data can image the seismically active region well. We compared tomography results with fixed seismic event locations against those with updated event locations. Tomography results with updated event locations showed better fits to the observations and improved the

seismic event catalog, showing sharper patterns compared to the original one. These patterns helped us monitor the seismically active fractures since the seismic events were mostly due to hydraulic stimulations. Two parallel fractures revealed by the updated seismic event catalog spatially correlated with independent borehole temperature observations. The average seismic velocity values of the well-constrained volume agreed to the first order with core sample measurements and active-source seismic surveys.

INTRODUCTION

Enhanced geothermal systems (EGS) have the potential to significantly expand the usage of geothermal energy with cutting-edge subsurface engineering techniques. To ensure EGS operate as safely and as economically as possible, high-resolution monitoring systems are required. To better understand EGS and develop required techniques, researchers from the EGS Collab project conducted hydraulic stimulations at the Sanford Underground Research Facility (SURF), located in Lead, South Dakota (Kneafsey et al., 2020). Experiment 1 of the project was carried out at the 4850-level of the facility, ~1.5 km beneath the surface. One important aspect of the experiment was to monitor newly generated and/or reactivated fractures due to hydraulic stimulations. Seismic monitoring was one of the primary diagnostic tools we used to monitor these fractures. Precise locations of seismic events improve our ability to not only quantify the geometry and orientation of individual fractures but also study interactions between multiple fractures.

Seismic tomography has been routinely performed for global (e.g., Moulik and Ekström, 2014), regional (e.g., Maceira and Ammon, 2009; Chai et al., 2015; Syracuse et al., 2016, 2017), and local (e.g., Zhang and Thurber, 2003; Syracuse et al., 2015; Qian et al., 2018) applications. However, few publications have focused on meter-scale (resolution) tomography largely due to the scarcity of suitable data. Passive seismic data recorded during Experiment 1 of the EGS Collab project provided a rare opportunity to conduct seismic tomography at meter-scale resolution. Hydraulic fractures on the order of 10-meter radius were stimulated in a phyllite rock mass and monitored at distances ranging from about 6 to 20 m away from the seismic activity (Kneafsey et al., 2020). An original seismic event catalog that was generated with a homogeneous seismic velocity model is available (Schoenball et al., 2020). Double difference methods have been widely used to improve seismic event locations (e.g., Waldhauser and Ellsworth, 2000; Wolfe, 2002). Published results (e.g., Zhang and Thurber, 2003; Roecker et al., 2006) show that simultaneously determining seismic event locations and subsurface velocity structure can improve event location accuracy and precision. We used a double-difference tomography package (tomoDD; see Zhang and Thurber, 2003, 2006) to image the subsurface seismic structure and update the seismic event catalog. The seismic events were the results of multiple hydraulic stimulations, carried out between May and December 2018, from three separate intervals in the injection well. Evidence indicated that events were caused both by the propagation of new hydraulic fractures and by the activation of natural fractures exist in the catalog (Fu et al., 2020).

DATA AND METHODOGY

We used seismic arrival times from both P and S waves to update the seismic event locations and image the subsurface seismic structure simultaneously. Previous studies have shown fixing the seismic event location during seismic tomography leads to bias in velocity anomalies (Thurber, 1992). We performed seismic tomography with the seismic event location fixed as the control group. Figure 1 shows the layout of eight ~60-meter-long boreholes comprised of one injection, one production, and six monitoring wells. Seismic sensors, including 24 hydrophones (single component) and 12 three-component accelerometers, were deployed in the monitoring wells. The seismic data that we used were recorded with a sampling rate of 100 kHz. As shown in Figure 2, the dominant frequency of the recorded seismic signal is around 3-20 kHz. Microseismic events were detected from the seismic recordings using a standard STA/LTA algorithm (Allen, 1978). Initially, P-wave arrivals were obtained automatically using the PhasePAPy package (Chen and Holland, 2016). The P-wave arrival times were reviewed and reprocessed manually to remove problematic picks and improve accuracy. S-wave arrival times were added manually when the signal was acceptable. Hypoinverse (Klein, 2002) was then used to invert for the seismic event locations and origin times. Details about the initial seismic event catalog and seismic phase picking can be found in Schoenball et al. (2020). The original catalog with refined seismic arrival times, and a homogeneous starting model (a P-wave velocity of 5.9 km/s and an S-wave velocity of 3.5 km/s as measured by fitting traveltime curves in Figure 3), were fed into a modified version of the tomoDD package (Zhang and Thurber, 2003, 2006) to simultaneously image the 3D seismic structure and improve the seismic event locations and origin times.

A total of 18,543 P-wave and 8,935 S-wave phase picks (arrival times) from 1,874 seismic events were used in the tomography. Travel-time curves for both P and S waves are shown in Figure 3. A large portion of the P-wave observations indicates an apparent velocity (source-receiver distance over travel-time) of approximately 5.9 km/s. Most S-wave observations show an apparent velocity of approximately 3.5 km/s. Considering the geological variations of the study area imaged from an active-source survey (Schwering et al., 2018) and uncertainties in seismic event locations (Schoenball et al., 2020), we excluded P-wave picks (6% of the total) with an apparent velocity larger than 8 km/s and smaller than 4 km/s during the inversions. Both the catalog picks and catalog differential times (travel time differences between event pairs) were used in the inversions. We performed two sets of tomographic inversions. For the first set, seismic event locations were held fixed at the original locations during the inversion. The seismic event locations were allowed to change for the second set of inversions. For each set, we ran the inversions 100 times with different regularization weights (smoothing and damping) since previous studies demonstrated that these regularization weights affect the inversion results (e.g., Maceira and Ammon, 2009; Chai et al., 2015, 2019; Syracuse et al., 2015, 2016, 2017). The smoothing weight controls the smoothness of the velocity model, whereas the damping weight controls the inversion stability (Zhang and Thurber, 2003). Specifically, the smoothness constraints were computed with a first-difference matrix. An L-curve analysis (e.g., Hansen, 1992) was used to identify the best set of weights. The velocity models and seismic event locations were visually inspected with interactive visualizations similar to Chai et al. (2018).

Synthetic tests

Due to the uneven distribution of seismic events and nonuniform sensor geometry, the quantity of the available constraints varied within the study area. We use synthetic tests to quantify the volume that was well-constrained by observations. Standard checkerboard tests were performed with different anomaly sizes. We found that the finest resolvable unit had an anomaly size of 1 m^3. Using the average seismic velocity, the range of recorded travel times, dominant frequency of the seismic signal, and the formula from Chai et al. (2020), the estimated first Fresnel zone width spans from 1 to 4 meters (Text S1). Since both the checkerboard tests and the first Fresnel zone width calculation suggest that the minimum resolution is 1 m^3, we discretize the study area with 1 m^3 cubes. The synthetic P-wave velocity (V_p) model consists of alternating fast and slow anomalies with a V_p of 6.2 km/s (5% faster than the average V_p that was measured from P-wave travel-time curves) and 5.6 km/s (5% slower), respectively. The synthetic S-wave velocity (V_s) model was computed from the V_p model with a V_p/V_s ratio of 1.69 estimated from the body-wave travel-time curves.

We computed P- and S-wave arrival times in these "checkerboard" models for each of the source-receiver pairs following the original observations. Starting with a homogeneous 3D velocity model with a P-wave speed of 5.9 km/s and an S-wave speed of 3.5 km/s, we used the simulated seismic arrival times and the original seismic event catalog to invert for the seismic structure. Seismic event locations were initialized at the inverted locations from the optimal inversion of the real data for these checkerboard tests (see the following section for details). We allow the seismic event locations to change during the inversion for these checkerboard tests. Figure 4 shows slices of the recovered P-wave and S-wave velocity. The highlighted area indicates the recovered velocity is less than 0.1 km/s different from the true velocity for V_p or 0.06 km/s for V_s. A 3D spatial Gaussian filter with a width of 1 m in each direction was applied to the measured volume to remove small-scale (such as one or two cells) perturbations. As expected, the P-wave velocity structure was better constrained than the S-wave velocity structure. We were able to recover the P-wave velocity structure of the seismically active area reasonably well (Figure 4). As expected, when we fix the seismic sources at the inverted locations instead of allowing them to change, the well recovered volume is larger (see Figure S1).

RESULTS

When we fixed the seismic event locations, the optimal smoothing and damping weights were 5 and 1,000, respectively (Figure 5). In general, larger damping weights lead to better fits with observations for the same smoothing weight, which might be due to the fact that the original catalog was computed with a homogenous velocity model. Inversions with smaller smoothing weights fit the data better than those with larger smoothing weights. If we allowed the seismic event locations to be updated during the tomographic inversion, the optimal smoothing and damping weights were 10 and 200, respectively (Figure 6). Inversions with damping weights smaller than 200 (same smoothing weight) resulted in similar data fits. We used default values of the tomoDD package for other parameters.

The inverted velocity models with the optimal weights show significant spatial variation for P and S waves and for both fixed and relocated seismic event sets of inversions (Figure 7 and Figure 8). The spatial variations show different patterns when we relocate the events compared to those with fixed event locations. Although it is difficult to interpret these spatial variations due to the small spatial scale of the volume, the velocity models obtained by simultaneously relocating the seismic events appear to be smoother and more coherent. The V_p model roughness as measured from first differences for the velocity model with seismic events relocated (0.007) is smaller than that of the velocity model with seismic event locations fixed (0.027). The V_s model roughness for the velocity model with seismic events relocated (0.0017) is also smaller than that of the velocity model with seismic event locations fixed (0.0041).

We also used more objective and quantifiable metrics in the following to compare the velocity models with seismic events relocated or fixed. The updated event locations for stimulations in May 22-25, June 25, and December 21-22, 2018 were compared with the original event locations in Figure 9. Details of these stimulations can be found in Schoenball et al. (2020). The updated event locations show a sharper pattern (i.e., tighter alignments of the events) than the original locations. Updated event locations associated with stimulations in May 2018 indicate two parallel fracture planes that are not obvious in the original seismic event catalog. These two parallel fracture planes were confirmed by independent borehole temperature measurements using distributed fiber sensing with 0.25 m spatial resolution – the hydraulic fracture intersections manifested as localized temperature anomalies (Fu et al., 2020). The intercepted borehole is identified in Figure 9.

DISCUSSION

As with any nonlinear inversion problem, the choice of inversion parameters (i.e., smoothing and damping) affects the fit to the data as well as the smoothness of the resulting velocity models (Figure 5 and Figure 6). However, allowing the original seismic events locations to be updated during the inversion results in better overall data fits to both P- and S-wave travel times for most of the inversion parameters (Figure 10). When we focus on the two inversions with the optimal inversion parameters, the distributions of final P- and S-wave residuals do not differ significantly from those of the starting homogeneous model when the events are fixed at the original locations (Figure 11). On the other hand, there is a noticeable reduction in both P- and S-wave residuals when we allow the event locations to change. The final P- and S-wave residuals are centered at zero. Most of the residuals for the final velocity model are smaller than 0.2 milliseconds for both P and S waves. The inverted velocity model fits the data for individual seismic events better than the homogeneous model and the original event locations (Figure 12). We also relocated the seismic events using the double-difference measurements but without inverting the seismic velocity models (Figure S2). The update seismic catalog obtained using a fixed homogeneous velocity model shows the planar features better than those for the original locations but not as tight as those for the seismic locations inverted simultaneously. As expected, the misfit to both P- and S-wave measurements is larger when we do not invert the seismic velocity models (Figure S3).

The median P- and S-wave velocity of the well-constrained volume from the inversion with event locations fixed is the same as that from the inversion with event locations updated (Figure 13). The average velocity is 5.9 km/s for P-waves and 3.5 km/s for S-waves, which agrees to first order with core sample measurements (Oldenburg et al., 2016; Condon, 2019; Philip et al., 2019). The spread of P- and S-wave velocity values from our velocity model are larger when we fix the event locations compared to those when we update the event locations (Figure 13). One plausible explanation is that errors in event locations were translated into erroneous velocity variations when we fix the events to the original locations. We also compared seismic-data-derived P- and S-wave velocities that are colocated (within 2 m radius) with the core samples analyzed by Condon (2019). Due to the anisotropic nature of the testbed and spatial heterogeneities, P- and S-wave velocities measured from core samples (Condon, 2019), derived from passive seismic recordings, and the baseline velocity model from an active source survey (Schwering et al., 2018) change over wide ranges. Numeric studies (e.g., Barbosa et al., 2017) suggest both hydraulic and elastic anisotropy (of the host rock) contribute to the observed anisotropy, which lead to large variations in seismic velocities. Accounting for anisotropic properties is beyond the scope of this study; Gao et al. (2020) focus on the anisotropic structure for the study area. Figure 14 shows a comparison of the baseline velocity model derived from the active-source survey (Schwering et al., 2018), the reprocessed velocity model of the same active-source survey, and the velocity model from our inversion. The reprocessed velocity model was obtained by using the fat-ray inversion method (Jordi et al., 2016). The travel time computations used the open source E4D code and an unstructured tetrahedral mesh as described by Lelièvre et al. (2011). Our velocity model shows a slightly higher resolution compared to that from the active-source data for the seismically active volume as evidenced by the smaller spatial scale of the velocity anomalies. The resolution difference is largely due to differences in source-receiver distribution. The 2D velocity models from the active source survey were constrained with data from two near-parallel boreholes. Our 3D velocity model is obtained with data from a 3D monitoring system. An independent 3D velocity model has been processed from the active-source data (not shown here, see Schwering et al., 2018). However, the 3D active-source derived model does not overlap spatially with our 3D velocity model due to source-sensor location differences. The main frequency of the active sources is much lower than that for our data. The range of velocity anomalies of our velocity model is smaller, which may be due to anisotropy (different ray path orientations with respect to the foliation of the host rock for passive and active-source data). The seismic event location changes are generally on the order of one meter (Figure 15), which is consistent with uncertainty estimates of the original seismic event catalog (Schoenball et al., 2020). The average event origin time change is 14 microseconds.

CONCLUSIONS

We performed meter-scale double-difference tomography for the EGS Collab project at SURF using seismic data. Two sets of inversions were carried out: one with fixed event locations (at the original locations) and the other with event location updated during the inversion. As expected, simultaneously inverting for the seismic velocity structure and seismic events locations leads to a better fit of the observations than fixing the seismic event locations or fixing the velocity model. The relocated events show sharper fracture patterns compared to the original locations. Moreover, two parallel alignments associated with the May 2018 stimulations were validated with complementary constraints provided by independent borehole temperature observations. Checkerboard tests show we can image the seismically active region reasonably well. The well-constrained volume for P-waves is larger than that for S-waves. The average P- and S-wave velocity values for the well-constrained volume agree with other independent measurements to first order.

Our results suggest that double-difference tomography can considerably improve the accuracy of the seismic event catalog at meter scales, which in turn helps us better constrain the fracture system at the Experiment 1 site of the EGS Collab project. A more precise catalog helps us to better investigate the evolution of the fracture system. A more detailed structure of the fracture system not only helps us more thoroughly analyze the interaction between different fractures but also provides valuable constraints to various numerical simulations that are being conducted. Detailed subsurface elastic property models can also be used to estimate 3D stress models (e.g., Chai et al., 2021). Since the double-difference tomography technique has been widely used for areas with spatial scales from a few kilometers to several hundreds of kilometers, our results reassure that double-different tomography can be utilized at various scales. Similar to previous EGS applications (e.g., Charléty et al., 2006; Kraft and Deichmann, 2014), our results suggest that double-different tomography should be suitable for other EGS projects such as the Utah Frontier Observatory for Research in Geothermal Energy (FORGE, Moore et al., 2020), the Bedretto Underground Laboratory for Geoenergies in Switzerland (Gischig et al., 2019), and the Grimsel Test Site in Switzerland (Dutler et al., 2020). As in larger-scale studies, taking into account the spatial variation in seismic velocities leads to better seismic event locations at meter scales. We suggest accounting for seismic heterogeneities in seismic event location studies if the data are abundant. Double-different tomography can be used together with deep learning phase pickers to further improve the seismic event catalog and velocity structure (Chai et al., 2020).

DATA AND RESOURCES

The original seismic event catalog and seismograms were obtained from EGS Collab data available on the Geothermal Data Repository at https://dx.doi.org/10.15121/1557417 (Schoenball et al., 2019, last accessed in June 2021). The seismic velocity model derived from active-source surveys can be accessed from EGS Collab data at https://dx.doi.org/10.15121/1497682 (Schwering et al., 2018, last accessed in February 2020) . Some plots were made using Plotly (https://plot.ly/, last accessed in February 2020) and Matplotlib (Hunter, 2007). ObsPy (Beyreuther et al., 2010; Megies et al., 2011; Krischer et al., 2015) and Numpy (van der Walt et al., 2011) were used to process or analyze the data. The Generic Mapping Tools (GMT, Wessel et al., 2013) was used to generate Figure 14. The seismic velocity models, updated seismic event catalog, and associated visualizations can be accessed at https://dx.doi.org/10.15121/1642468 (last accessed in June 2021). The E4D code can be accessed at https://e4d.pnnl.gov (last accessed in June 2021).

ACKNOWLEDGEMENTS

This material was based upon work supported by the U.S. Department of Energy, Office of Energy Efficiency and Renewable Energy (EERE), Office of Technology Development, Geothermal Technologies Office, under Award Number DE-AC05-00OR22725 with Oak Ridge National Laboratory, and under Award Number DE-AC52-07NA27344 with Lawrence Livermore National Laboratory. Sandia National Laboratories is a multimission laboratory managed and operated by National Technology & Engineering Solutions of Sandia, LLC, a wholly owned subsidiary of Honeywell International Inc., for the U.S. Department of Energy's National Nuclear Security Administration under contract DE-NA0003525. This paper describes objective technical results and analysis. Any subjective views or opinions that might be expressed in the paper do not necessarily represent the views of the U.S. Department of Energy or the United States Government. The United States Government retains, and the publisher, by accepting the article for publication, acknowledges that the United States Government retains a non-exclusive, paid-up, irrevocable, world-wide license to publish or reproduce the published form of this manuscript, or allow others to do so, for United States Government purposes. The research supporting this work took place in whole or in part at the Sanford Underground Research Facility in Lead, South Dakota. The assistance of the Sanford Underground Research Facility and its personnel in providing physical access and general logistical and technical support is acknowledged. We thank Haijiang Zhang for sharing the tomoDD package. We acknowledge Yarom Polsky for helpful discussions. We thank the Editor Thomas Pratt, an associate editor, and two anonymous reviewers for their constructive comments. The authors declare that they have no conflict of interest. The authors declare that they have no known competing financial interests or personal relationships that could have appeared to influence the work reported in this paper.

REFERENCES

Allen, R. V., 1978, Automatic earthquake recognition and timing from single traces, Bull. Seismol. Soc. Am., 68, no. 5, 1521–1532.

Barbosa, N. D., J. G. Rubino, E. Caspari, and K. Holliger, 2017, Sensitivity of Seismic Attenuation and Phase Velocity to Intrinsic Background Anisotropy in Fractured Porous Rocks: A Numerical Study, J. Geophys. Res. Solid Earth, 122, no. 10, 8181–8199, doi: 10.1002/2017JB014558.

Beyreuther, M., R. Barsch, L. Krischer, T. Megies, Y. Behr, and J. Wassermann, 2010, ObsPy: A Python Toolbox for Seismology, Seismol. Res. Lett., 81, no. 3, 530–533, doi: 10.1785/gssrl.81.3.530.

Chai, C., C. J. Ammon, M. Maceira, and R. B. Herrmann, 2018, Interactive Visualization of Complex Seismic Data and Models Using Bokeh, Seismol. Res. Lett., 89, no. 2A, 668–676, doi: 10.1785/0220170132.

Chai, C., C. J. Ammon, M. Maceira, and R. B. Herrmann, 2015, Inverting interpolated receiver functions with surface wave dispersion and gravity: Application to the western U.S. and adjacent Canada and Mexico, Geophys. Res. Lett., 42, no. 11, 4359–4366, doi: 10.1002/2015GL063733.

Chai, C., A. A. Delorey, M. Maceira, W. Levandowski, R. A. Guyer, H. Zhang, D. Coblentz, and P. A. Johnson, 2021, A 3D Full Stress Tensor Model for Oklahoma, J.

Geophys. Res. Solid Earth, 126, no. 4, e2020JB021113, doi: 10.1029/2020JB021113.

Chai, C., M. Maceira, H. Santos-Villalobos, and E. C. Team, 2019, Subsurface Seismic Structure Around the Sanford Underground Research Facility, in *44th Workshop on Geothermal Reservoir Engineering*, 1364–1376.

Chai, C., M. Maceira, H. J. Santos-Villalobos, S. V. Venkatakrishnan, M. Schoenball, W. Zhu, G. C. Beroza, C. Thurber, and EGS Collab Team, 2020, Using a Deep Neural Network and Transfer Learning to Bridge Scales for Seismic Phase Picking, Geophys. Res. Lett., 47, no. 16, e2020GL088651, doi: 10.1029/2020GL088651.

Charléty, J., N. Cuenot, C. Dorbath, and L. Dorbath, 2006, Tomographic study of the seismic velocity at the Soultz-sous-Forêts EGS/HDR site, Geothermics, 35, nos. 5–6, 532–543, doi: 10.1016/j.geothermics.2006.10.002.

Chen, C., and A. A. Holland, 2016, PhasePApy: A Robust Pure Python Package for Automatic Identification of Seismic Phases, Seismol. Res. Lett., 87, no. 6, 1384–1396, doi: 10.1785/0220160019.

Condon, K., 2019, Mechanical Properties of Poorman schist and Westerly granite, University of Wisconsin-Madison.

Dutler, N. O., B. Valley, L. Villiger, V. Gischig, and F. Amann, 2020, Observation of a repeated step-wise fracture growth during hydraulic fracturing experiment at the Grimsel Test Site, in *World Geothermal Conference 2020*, 1–10.

Fu, P., H. Wu, X. Ju, and J. Morris, 2020, Analyzing Fracture Flow Channel Area in EGS Collab Experiment 1 Testbed, in *45th Workshop on Geothermal Reservoir Engineering*, 1283–1292.

Gao, K., L. Huang, H. A. Knox, P. C. Schwering, C. R. Hoots, J. Ajo-franklin, T. J. Kneafsey, and EGS Collab Team, 2020, Anisotropic Elastic Properties of the First EGS Collab Testbed Revealed from the Campaign Cross-Borehole Seismic Data, in *45th Workshop on Geothermal Reservoir Engineering, Stanford, California*, 1293–1303.

Gischig, V., F. Bethmann, M. Hertrich, S. Wiemer, A. Mignan, M. Broccardo, L. Villiger, A. Obermann, and T. Diehl, 2019, Induced seismic hazard and risk analysis of hydraulic stimulation experiments at the Bedretto Underground Laboratory for Geoenergies (BULG).

Hunter, J. D., 2007, Matplotlib: a 2D graphics environment, Comput. Sci. Eng., 9, no. 3, 90–95, doi: 10.1109/MCSE.2007.55.

Jordi, C., C. Schmelzbach, and S. Greenhalgh, 2016, Frequency-dependent traveltime tomography using fat rays: application to near-surface seismic imaging, J. Appl. Geophys., 131, 202–213, doi: 10.1016/j.jappgeo.2016.06.002.

Klein, F. W., 2002, User’s Guide to HYPOINVERSE-2000, a Fortran Program to Solve for Earthquake Locations and Magnitudes, U.S. Geol. Surv. Open File Rep. 02-171, doi: http://geopubs.wr.usgs.gov/open-file/of02-171/.

Kneafsey, T. J. et al., 2020, The EGS Collab Project: Learning from Experiment 1, in *45th Workshop on Geothermal Reservoir Engineering, Stanford, California*, 1304–1318.

Kraft, T., and N. Deichmann, 2014, High-precision relocation and focal mechanism of the injection-induced seismicity at the Basel EGS, Geothermics, 52, 59–73, doi: 10.1016/j.geothermics.2014.05.014.

Krischer, L., T. Megies, R. Barsch, M. Beyreuther, T. Lecocq, C. Caudron, and J. Wassermann, 2015, ObsPy: A bridge for seismology into the scientific Python ecosystem, Comput. Sci. Discov., doi: 10.1088/1749-4699/8/1/014003.

Lelièvre, P. G., C. G. Farquharson, and C. A. Hurich, 2011, Computing first-arrival seismic traveltimes on unstructured 3-D tetrahedral grids using the Fast Marching Method, Geophys. J. Int., 184, no. 2, 885–896, doi: 10.1111/j.1365-246X.2010.04880.x.

Maceira, M., and C. J. Ammon, 2009, Joint inversion of surface wave velocity and gravity observations and its application to central Asian basins shear velocity structure, J. Geophys. Res., 114, no. B2, B02314, doi: 10.1029/2007JB005157.

Megies, T., M. Beyreuther, R. Barsch, L. Krischer, and J. Wassermann, 2011, ObsPy - what can it do for data centers and observatories?, Ann. Geophys., doi: 10.4401/ag-4838.

Moore, J., J. Mclennan, R. Allis, K. Pankow, S. Simmons, R. Podgorney, P. Wannamaker, J. Bartley, C. Jones, and W. Rickard, 2020, The Utah Frontier Observatory for Research in Geothermal Energy (FORGE): An International Laboratory for Enhanced Geothermal System Technology Development, in *45th Workshop on Geothermal Reservoir Engineering*, 481–490.

Moulik, P., and G. Ekström, 2014, An anisotropic shear velocity model of the Earth's mantle using normal modes, body waves, surface waves and long-period waveforms, Geophys. J. Int., 199, no. 3, 1713–1738, doi: 10.1093/gji/ggu356.

Oldenburg, C. M. et al., 2016, Intermediate-Scale Hydraulic Fracturing in a Deep Mine - kISMET Project Summary 2016, Berkeley, CA (United States).

Philip, L., N. James, J. William, and the EGS Collab Team, 2019, Geomechanical evaluation of natural shear fractures in the EGS Collab Experiment 1 test bed, in *53rd U.S. Rock Mechanics/Geomechanics Symposium*, ARMA-2019-1829.

Qian, J., H. Zhang, and E. Westman, 2018, New time-lapse seismic tomographic scheme based on double-difference tomography and its application in monitoring temporal velocity variations caused by underground coal mining, Geophys. J. Int., 215, no. 3, 2093–2104, doi: 10.1093/gji/ggy404.

Roecker, S., C. Thurber, K. Roberts, and L. Powell, 2006, Refining the image of the San Andreas Fault near Parkfield, California using a finite difference travel time computation technique, Tectonophysics, 426, nos. 1–2, 189–205, doi: 10.1016/j.tecto.2006.02.026.

Schoenball, M. et al., 2020, Creation of a Mixed-Mode Fracture Network at Mesoscale Through Hydraulic Fracturing and Shear Stimulation, J. Geophys. Res. Solid Earth, 125, no. 12, 1–21, doi: 10.1029/2020JB019807.

Schoenball, M. et al., 2019, Microseismic monitoring of meso-scale stimulations for the DOE EGS Collab project at the Sanford Underground Research Facility, in *44th Workshop on Geothermal Reservoir Engineering*, 1392–1399.

Schwering, P., K. Condon, H. A. Knox, D. Linneman, and C. R. Hoots, 2018, EGS Collab Testbed 1: Baseline Cross-well Seismic: <https://dx.doi.org/10.15121/1497682> (accessed December 1, 2019).

Syracuse, E. M., M. Maceira, G. A. Prieto, H. Zhang, and C. J. Ammon, 2016, Multiple plates subducting beneath Colombia, as illuminated by seismicity and velocity from the joint inversion of seismic and gravity data, Earth Planet. Sci. Lett., 444, 139–

149, doi: 10.1016/j.epsl.2016.03.050.

Syracuse, E. M., M. Maceira, H. Zhang, and C. H. Thurber, 2015, Seismicity and structure of Akutan and Makushin Volcanoes, Alaska, using joint body and surface wave tomography, J. Geophys. Res. Solid Earth, 120, no. 2, 1036–1052, doi: 10.1002/2014JB011616.

Syracuse, E. M., H. Zhang, and M. Maceira, 2017, Joint inversion of seismic and gravity data for imaging seismic velocity structure of the crust and upper mantle beneath Utah, United States, Tectonophysics, 718, 105–117, doi: 10.1016/j.tecto.2017.07.005.

Thurber, C. H., 1992, Hypocenter-velocity structure coupling in local earthquake tomography, Phys. Earth Planet. Inter., 75, nos. 1–3, 55–62, doi: 10.1016/0031-9201(92)90117-E.

Waldhauser, F., and W. L. Ellsworth, 2000, A Double-Difference Earthquake Location Algorithm: Method and Application to the Northern Hayward Fault, California, Bull. Seismol. Soc. Am., 90, no. 6, 1353–1368, doi: 10.1785/0120000006.

van der Walt, S., S. C. Colbert, and G. Varoquaux, 2011, The NumPy Array: A Structure for Efficient Numerical Computation, Comput. Sci. Eng., 13, no. 2, 22–30, doi: 10.1109/MCSE.2011.37.

Wessel, P., W. H. F. Smith, R. Scharroo, J. Luis, and F. Wobbe, 2013, Generic Mapping Tools: improved version released, Eos, Trans. Am. Geophys. Union, 94, no. 45, 409–410, doi: 10.1002/2013EO450001.

Wolfe, C. J., 2002, On the Mathematics of Using Difference Operators to Relocate Earthquakes, Bull. Seismol. Soc. Am., 92, no. 8, 2879–2892, doi: 10.1785/0120010189.

Zhang, H., and C. Thurber, 2006, Development and Applications of Double-difference Seismic Tomography, Pure Appl. Geophys., 163, nos. 2–3, 373–403, doi: 10.1007/s00024-005-0021-y.

Zhang, H., and C. Thurber, 2003, Double-difference tomography: the method and its application to the Hayward Fault, California, Bull. Seismol. Soc. Am., 93, no. 5, 1875–1889, doi: 10.1785/0120020190.

FULL MAILING ADDRESS FOR EACH AUTHOR

Chengping Chai, Oak Ridge National Laboratory, PO Box 2008, MS6075, Oak Ridge, TN 37831, USA, chaic@ornl.gov

Monica Maceira, Oak Ridge National Laboratory, PO Box 2008, MS6050, Oak Ridge, TN 37831, USA, maceiram@ornl.gov

Hector J. Santos-Villalobos, Oak Ridge National Laboratory, PO Box 2008, MS6418, Oak Ridge, TN 37831, USA, hsantos@ornl.gov

Singanallur V. Venkatakrishnan, Oak Ridge National Laboratory, PO Box 2008, MS6075, Oak Ridge, TN 37831, USA, venkatakrisv@ornl.gov

Martin Schoenball, Energy Geosciences Division, Lawrence Berkeley National Laboratory, MS74R316C, 1 Cyclotron Road, Berkeley, CA 94720, USA, schoenball@lbl.gov

Pengcheng Fu, Lawrence Livermore National Laboratory, 7000 East Avenue, L-286, Livermore, CA 94550, USA, fu4@llnl.gov

Clifford Thurber, Department of Geoscience, University of Wisconsin-Madison, 1215 West Dayton Street, Madison, WI 53706, USA, cthurber@wisc.edu

Paul C. Schwering, Sandia National Laboratories, PO Box 5800, MS 1033, Albuquerque, NM 87185, USA, pcschwe@sandia.gov

Timothy C. Johnson, Pacific Northwest National Laboratory, P.O. Box 999, MSIN K4-18, Richland, WA 99352 USA, TJ@pnnl.gov

Hunter A. Knox, Pacific Northwest National Laboratory, P.O. Box 999, MSIN K4-18, Richland, WA 99352 USA, hunter.knox@pnnl.gov

LIST OF FIGURE CAPTIONS

Figure 1. Borehole (thin lines) configuration and locations of the seismic sensors (dots) used. The thick gray line represents the drift located at the 4850-level (at a depth of 1.5 km from the surface) of the Sanford Underground Research Facility. The blue line indicates the injection well. The orange line represents the production well. Thin black lines are monitoring wells. The box shows the location of Figure 14. The black square represents the point (0, 0) in Figure 14. The black dot indicates the location of

core samples used in Figure 13. For interpretation of the color in this figure, please see the online version.

Figure 2. (a) An example seismogram recorded on May 23, 2018 with the P-wave and S-wave arrival time marked and (b) its spectrogram.

Figure 3. Travel-time curves for (a) P- and (b) S-waves. Dots represent body-wave phase picks. Lines stand for expected arrival times for different homogeneous velocity values. The original seismic event locations were used to compute the distances.

Figure 4. Slices of the recovered (a) P- and (b) S-wave seismic velocity model using data simulated with a checkerboard model. The source locations were allowed to change during the inversion. The highlighted area is better recovered. The dimmed area is not well constrained due to lack of data coverage. Colored lines are the same as in Figure 1. For interpretation of the color in this figure, please see the online version.

Figure 5. L-curve analysis results when seismic event locations are fixed at the original locations. The red open circle indicates the values corresponding to the selected optimal inversion parameters. The meaning of colors and symbols is the same in different panels. The model length is measured as the root mean square difference between the final velocity model and the initial model. The model roughness is calculated from the spatial derivatives of the final model. For interpretation of the color in this figure, please see the online version.

Figure 6. L-curve analysis results when seismic event locations are simultaneously updated. The red open circle indicates the values corresponding to the selected optimal inversion parameters. The meaning of colors and symbols is the same in different panels. The model length is measured as the difference between the final

velocity model and the initial model. The model roughness is calculated from the spatial derivatives of the final model. The axis range of each panel is different from those in Figure 5 to show detailed variations. For interpretation of the color in this figure, please see the online version.

Figure 7. Slices of inverted (a) P-wave and (b) S-wave seismic velocity models from the inversion with seismic event locations fixed at the original locations. The highlighted area is well-constrained. The dimmed area is not well-constrained due to lack of data coverage. Colored lines are the same as in Figure 1. For interpretation of the color in this figure, please see the online version.

Figure 8. Slices of inverted (a) P-wave and (b) S-wave seismic velocity models from the inversion with seismic event locations simultaneously updated. Colored lines are the same as in Figure 1. Animations with multiple cross-sections can be accessed with the link provided in the DATA AND RESOURCES section. For interpretation of the color in this figure, please see the online version.

Figure 9. Comparisons of original (a, c, and e) and updated (b, d, and f) seismic event locations (dots). (a) and (b) correspond to stimulations in May 2018. (c) and (d) correspond to stimulation in June 2018. (e) and (f) correspond to stimulations in December 2018. Colored lines are the same as in Figure 1. The thick line represents the intersected monitoring borehole. The dashed circles in (b) show the intersections. A 3D interactive visualization can be accessed with the link provided in the DATA AND RESOURCES section. A screen recording of the interactive visualization is provided as Video S1. For interpretation of the color in this figure, please see the online version.

Figure 10. (a) P-wave and (b) S-wave travel-time misfit distribution of inversions associated with different inversion parameters. Each count is associated with an inversion. The travel-time misfits were averaged among all available observations for each inversion. The purple bars are due to overlapping bins. For interpretation of the color in this figure, please see the online version.

Figure 11. Histograms showing (a and b) P-wave and (c and d) S-wave residuals for inversions with the optimal inversion parameters. The seismic event locations were fixed in (b) and (d). The event locations were relocated (a) and (c).

Figure 12. A comparison of data fit between the homogeneous velocity model and the inverted 3D velocity model for a seismic event that occurred on July 20, 2018. The dots represent the predicted arrival times using (a) the homogeneous velocity model and (b) the final 3D model. Vertical bars indicate the measured phase arrivals. The shaded boxes indicate the expected time windows that were computed with a velocity range of 4.9-6.9 km/s for P-waves and 2.9-4.1 km/s for S-waves. This is an extreme example. For many seismic events, the improvements in data fits are not so dramatic.

Figure 13. Absolute P-wave and S-wave velocity values for (left) the well-constrained volume (poorly constrained parts were excluded) and (right) near the core samples analyzed by Condon (2019). The location of the core samples is shown in Figure 1.

Figure 14. A comparison of P-wave velocity values on a plane obtained from a) a baseline model of an active seismic survey (Schwering et al., 2018), b) a reprocessed model of the active seismic survey, and c) the velocity model with seismic events relocated. The location of the plane is indicated in Figure 1. The open circles

represent seismic events within 0.5 meter of the plane. The dimmed area is not well constrained due to lack of data coverage. The dashed lines denote the boundary of the dimmed area. For interpretation of the color in this figure, please see the online version.

Figure 15. A histogram showing (a) the seismic event location changes and (b) origin time changes with respect to the original seismic event catalog. SD means standard derivation.

FIGURES

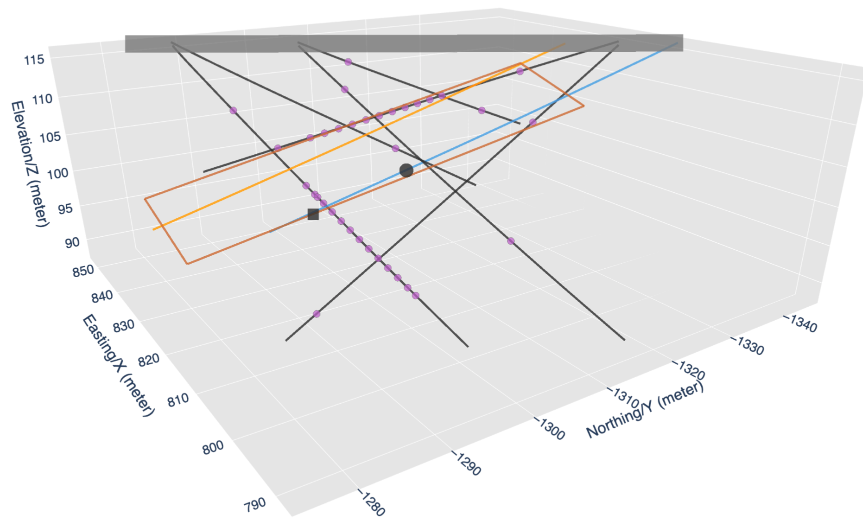

Figure 1. **Borehole (thin lines) configuration and locations of the seismic sensors (dots) used.** The thick gray line represents the drift located at the 4850-level (at a depth of 1.5 km from the surface) of the Sanford Underground Research Facility. The blue line indicates the injection well. The orange line represents the production well. Thin black lines are monitoring wells. The box shows the location of Figure 14. The black square represents the point (0, 0) in Figure 14. The black dot indicates the location of core samples used in Figure 13. For interpretation of the color in this figure, please see the online version.

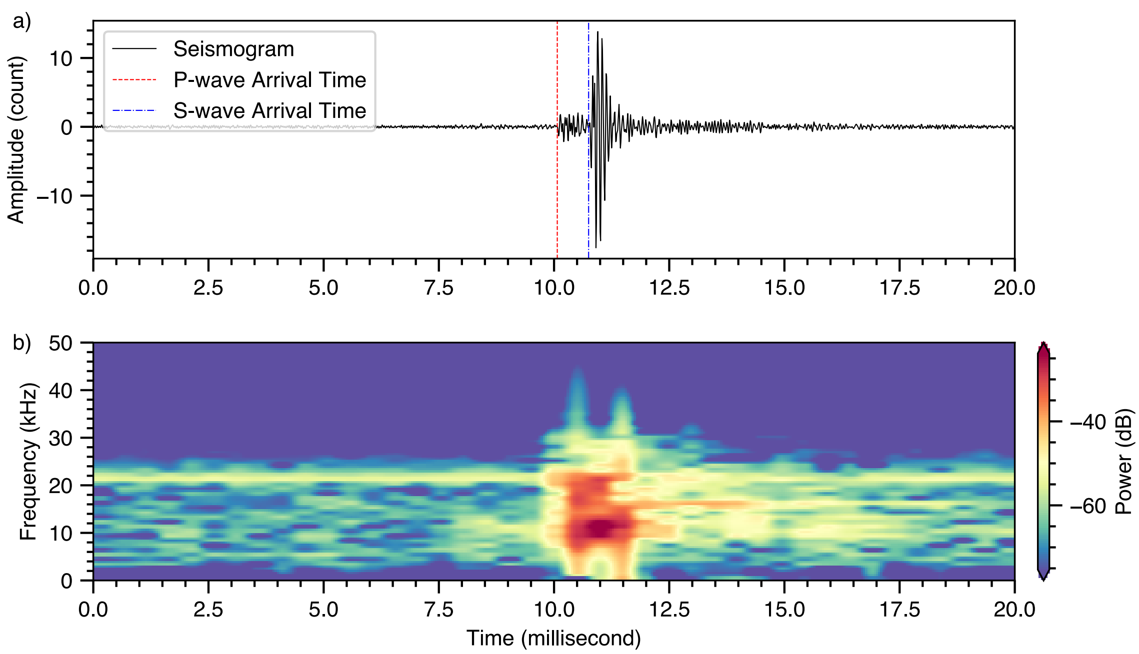

Figure 2. (a) An example seismogram recorded on May 23, 2018 with the P-wave and S-wave arrival time marked and (b) its spectrogram.

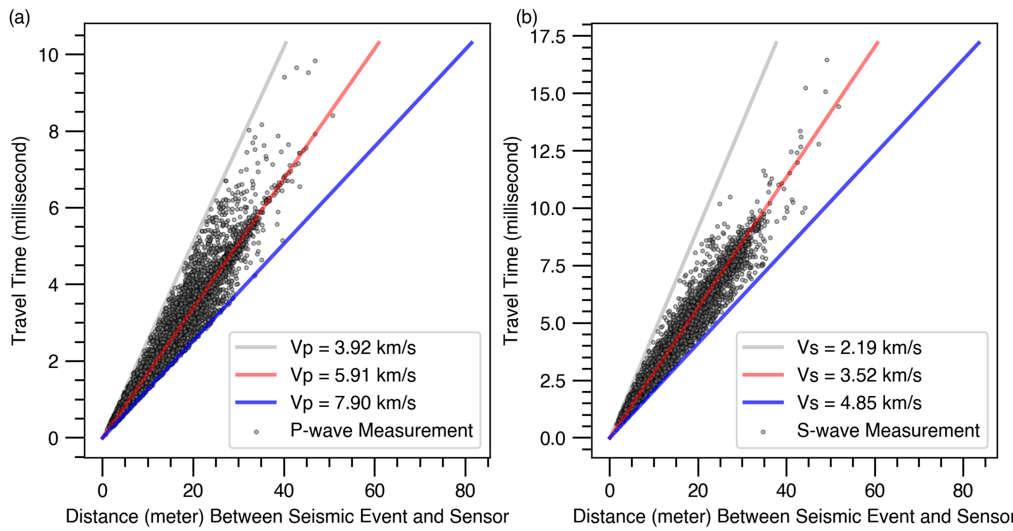

Figure 3. Travel-time curves for (a) P- and (b) S-waves. Dots represent body-wave phase picks. Lines stand for expected arrival times for different homogeneous velocity values. The original seismic event locations were used to compute the distances.

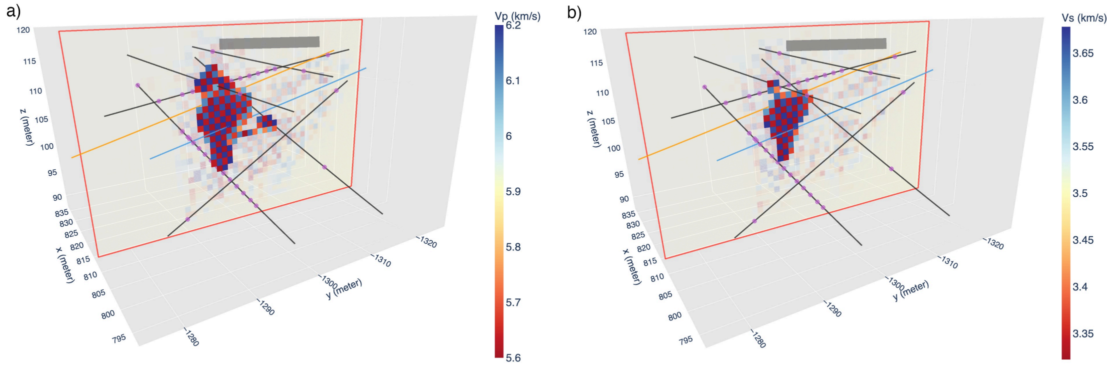

Figure 4. Slices of the recovered (a) P- and (b) S-wave seismic velocity model using data simulated with a checkerboard model. The source locations were allowed to change during the inversion. The highlighted area is better recovered. The dimmed area is not well constrained due to lack of data coverage. Colored lines are the same as in Figure 1. For interpretation of the color in this figure, please see the online version.

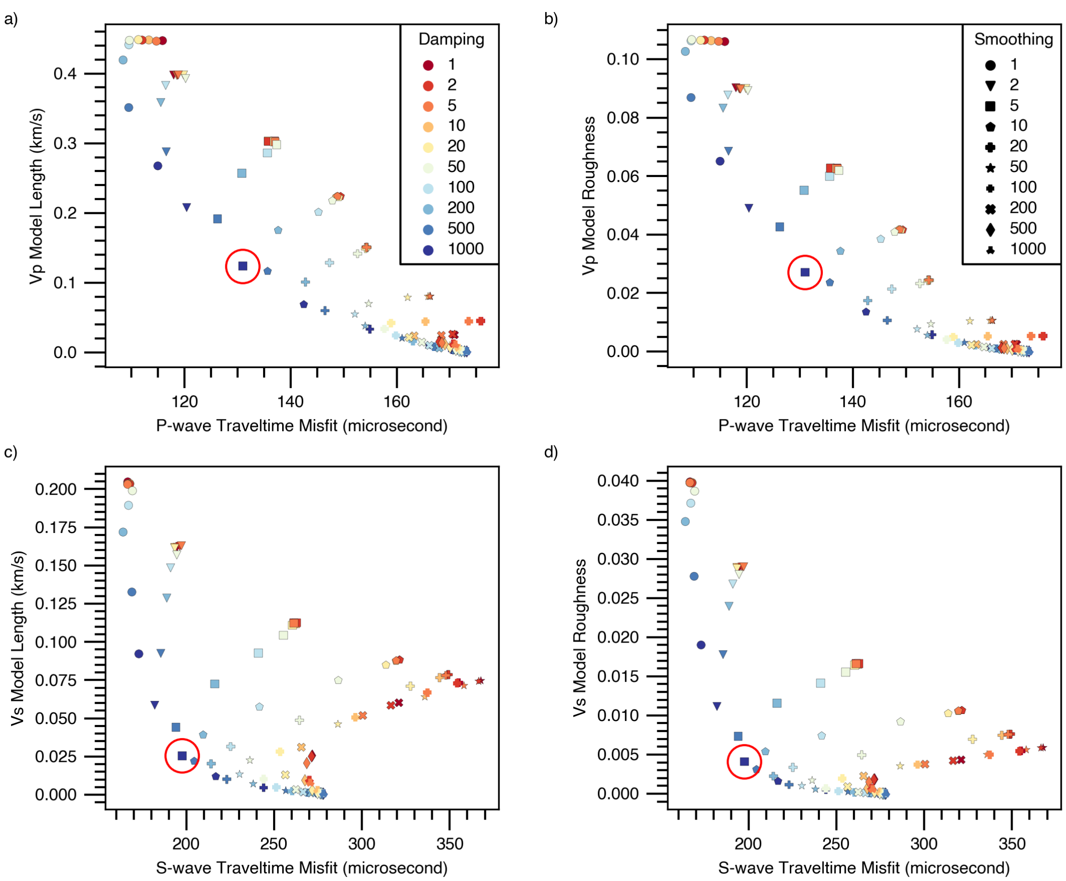

Figure 5. L-curve analysis results when seismic event locations are fixed at the original locations. The red open circle indicates the values corresponding to the selected optimal inversion parameters. The meaning of colors and symbols is the same in different panels. The model length is measured as the root mean square difference between the final velocity model and the initial model. The model roughness is calculated from the spatial derivatives of the final model. For interpretation of the color in this figure, please see the online version.

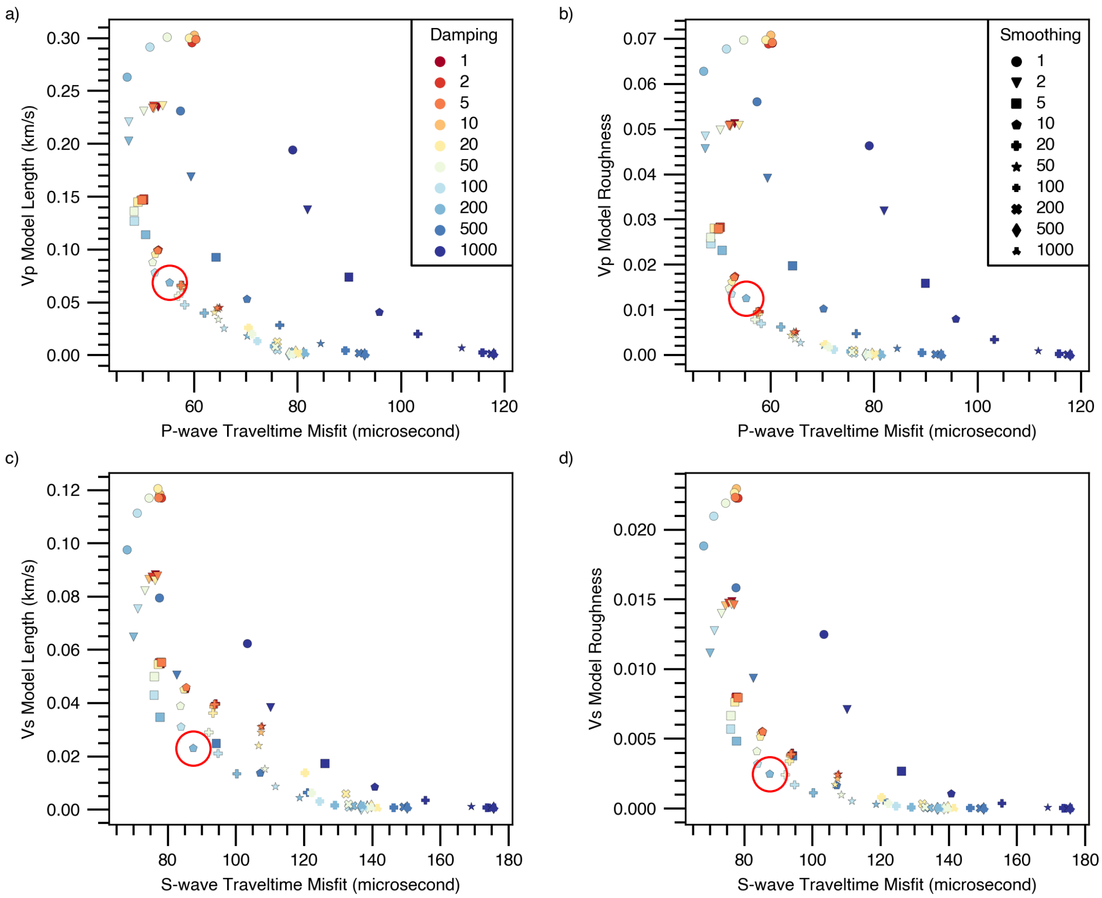

Figure 6. L-curve analysis results when seismic event locations are simultaneously updated. The red open circle indicates the values corresponding to the selected optimal inversion parameters. The meaning of colors and symbols is the same in different panels. The model length is measured as the difference between the final velocity model and the initial model. The model roughness is calculated from the spatial derivatives of the final model. The axis range of each panel is different from those in Figure 5 to show detailed variations. For interpretation of the color in this figure, please see the online version.

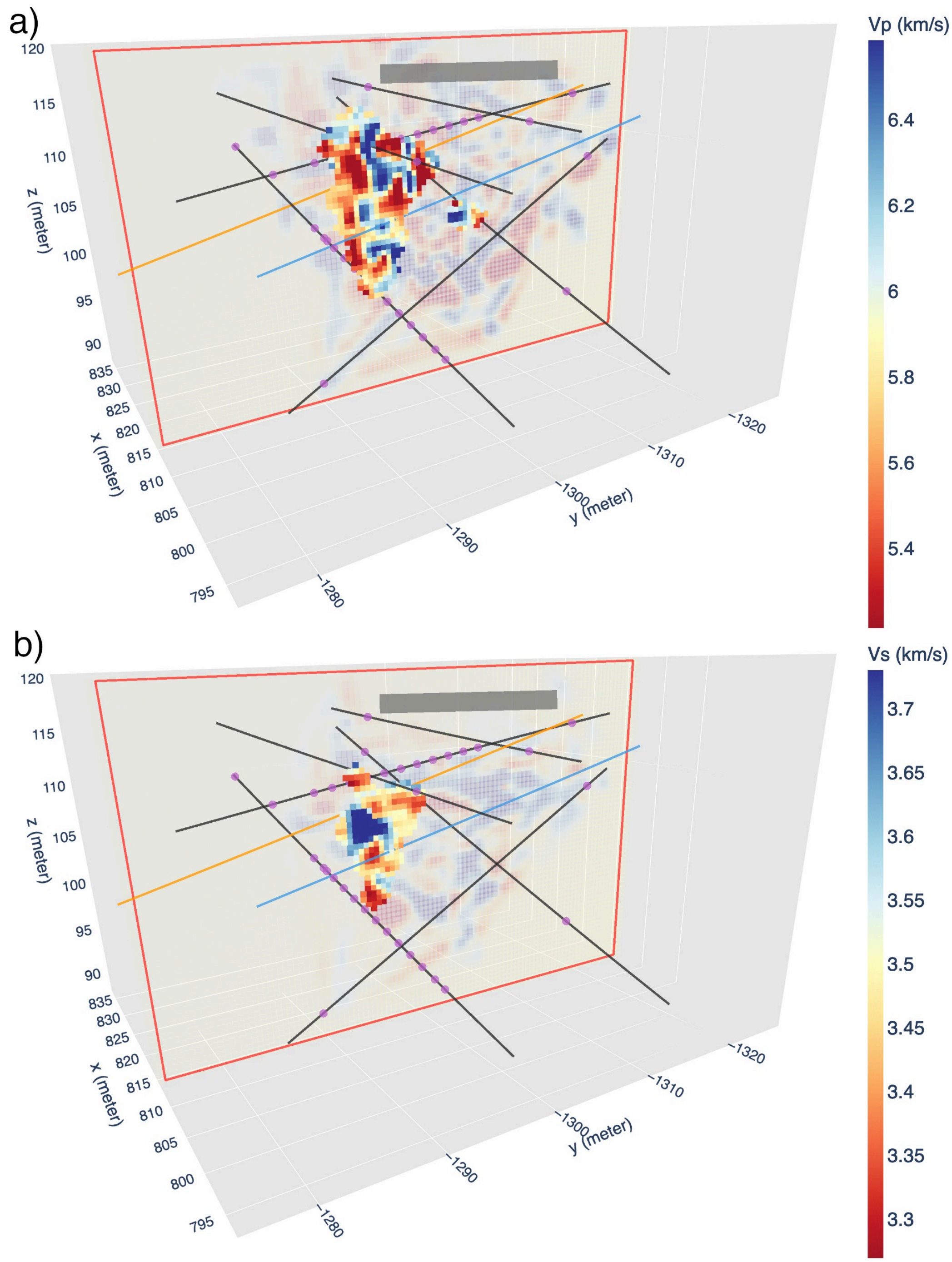

Figure 7. Slices of inverted (a) P-wave and (b) S-wave seismic velocity models from the inversion with seismic event locations fixed at the original locations. The highlighted area is well-constrained. The dimmed area is not well-constrained due to lack of data coverage. Colored lines are the same as in Figure 1. For interpretation of the color in this figure, please see the online version.

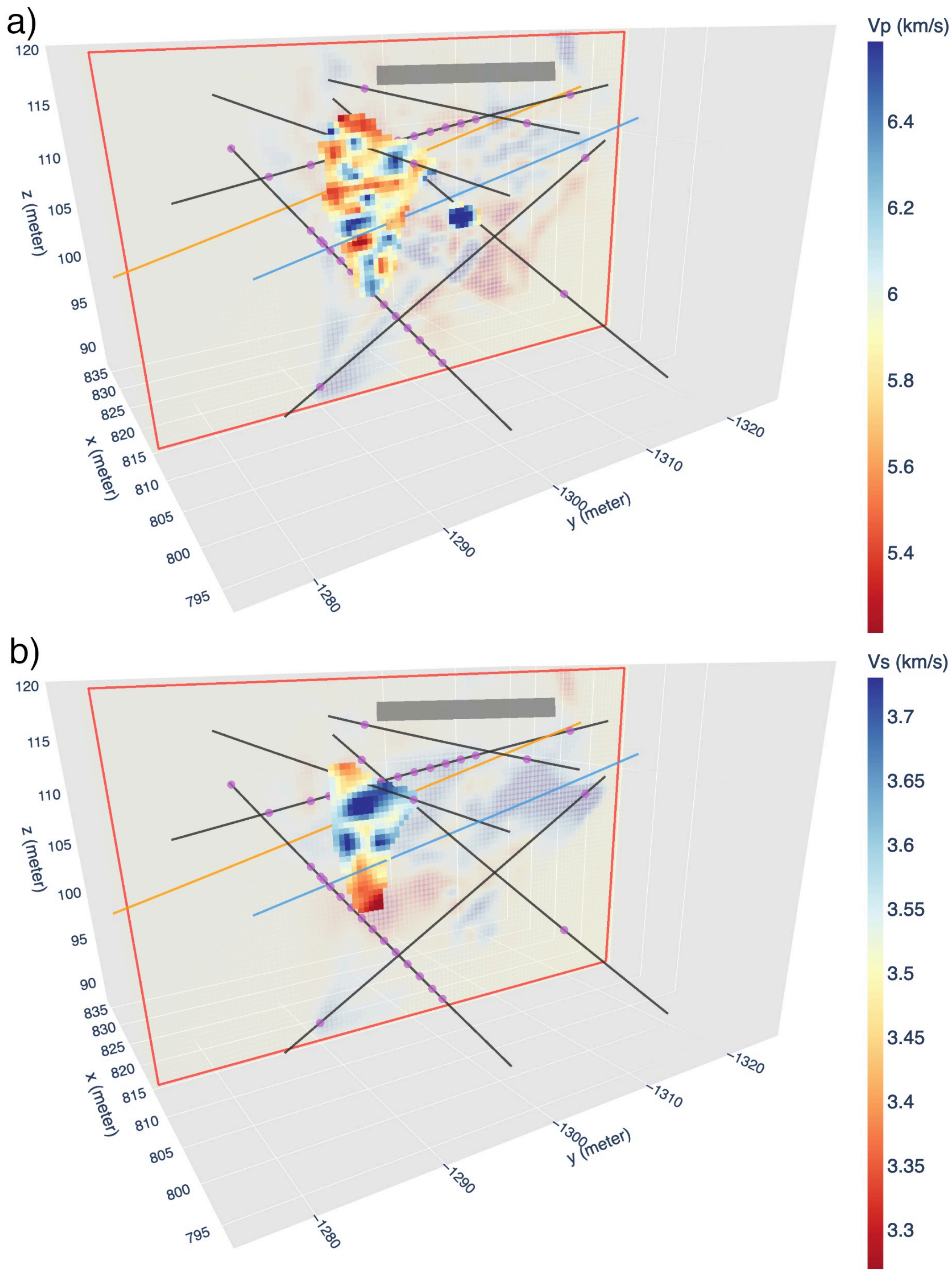

Figure 8. Slices of inverted (a) P-wave and (b) S-wave seismic velocity models from the inversion with seismic event locations simultaneously updated. Colored lines are the same as in Figure 1. Animations with multiple cross-sections can be accessed with the link provided in the DATA AND RESOURCES section. For interpretation of the color in this figure, please see the online version.

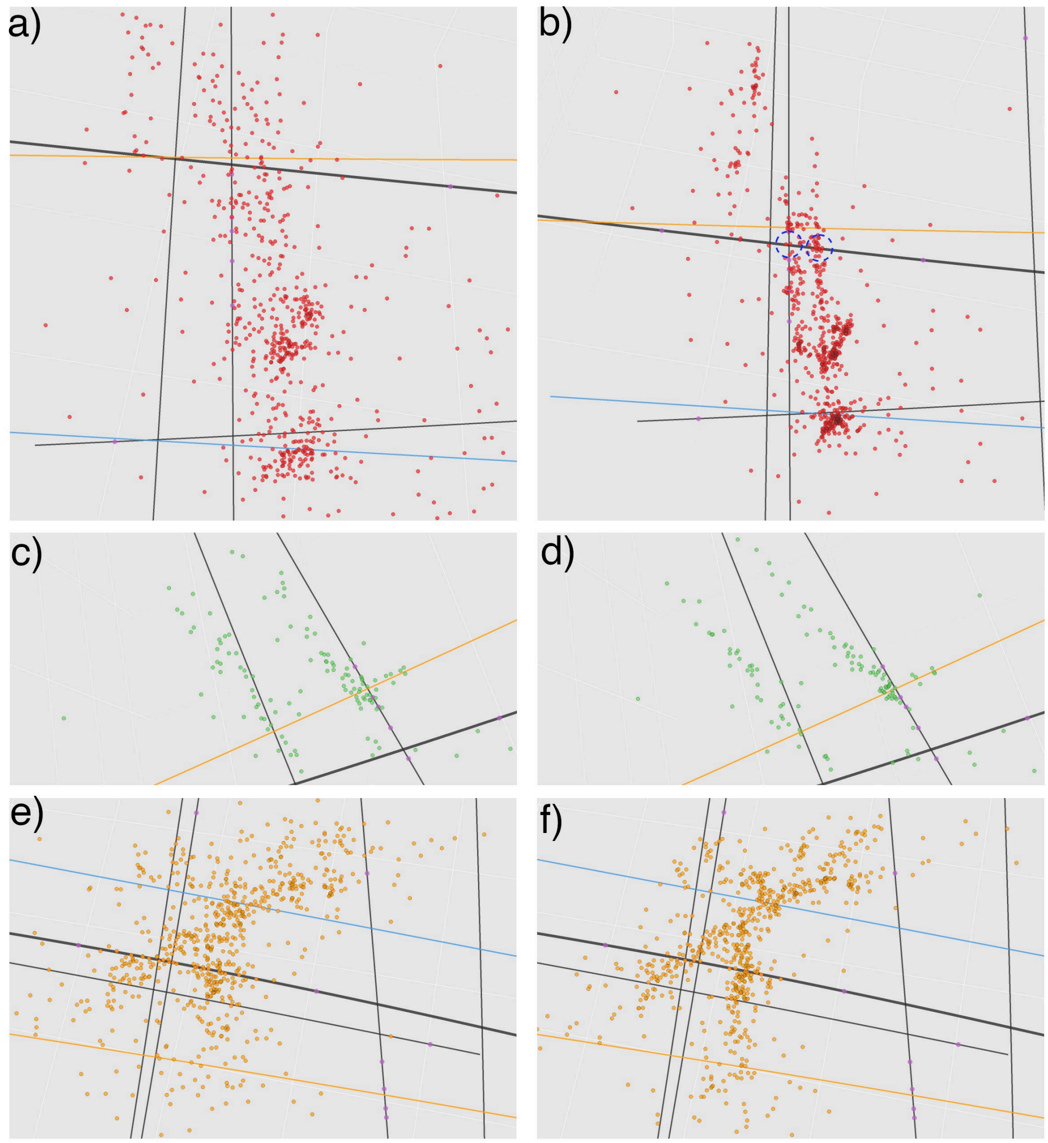

Figure 9. Comparisons of original (a, c, and e) and updated (b, d, and f) seismic event locations (dots). (a) and (b) correspond to stimulations in May 2018. (c) and (d) correspond to stimulation in June 2018. (e) and (f) correspond to stimulations in December 2018. Colored lines are the same as in Figure 1. The thick line represents the intersected monitoring borehole. The dashed circles in (b) show the intersections. A 3D interactive visualization can be accessed with the link provided in the DATA AND RESOURCES section. A screen recording of the interactive visualization is provided as Video S1. For interpretation of the color in this figure, please see the online version.

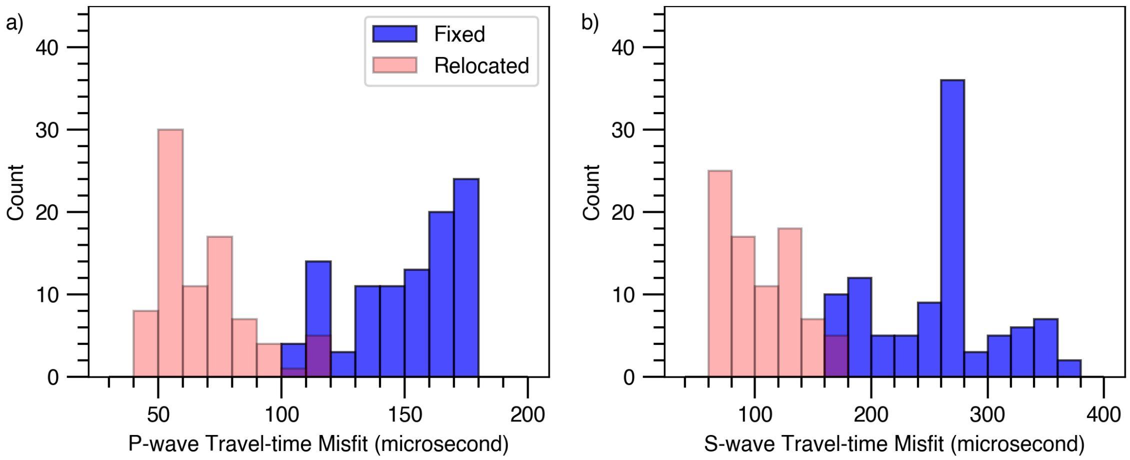

Figure 10. (a) P-wave and (b) S-wave travel-time misfit distribution of inversions associated with different inversion parameters. Each count is associated with an inversion. The travel-time misfits were averaged among all available observations for each inversion. The purple bars are due to overlapping bins. For interpretation of the color in this figure, please see the online version.

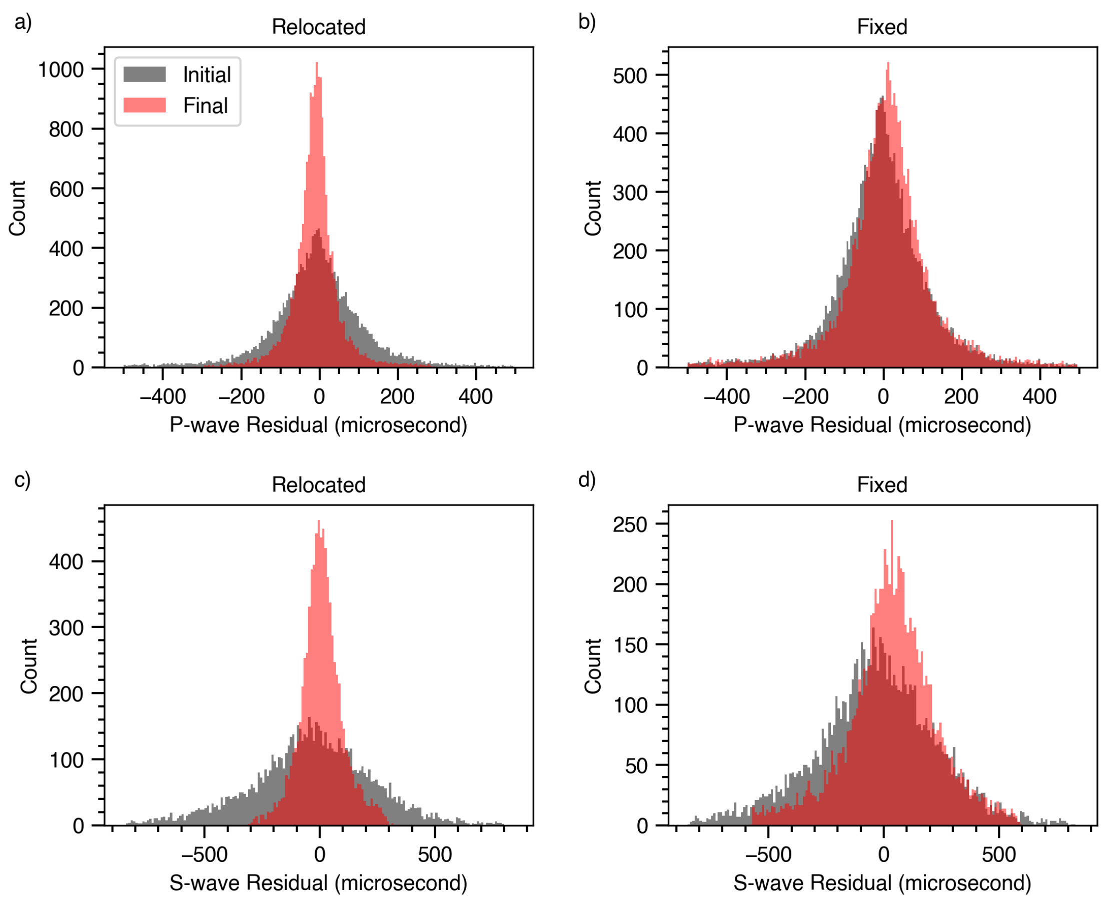

Figure 11. Histograms showing (a and b) P-wave and (c and d) S-wave residuals for inversions with the optimal inversion parameters. The seismic event locations were fixed in (b) and (d). The event locations were relocated (a) and (c).

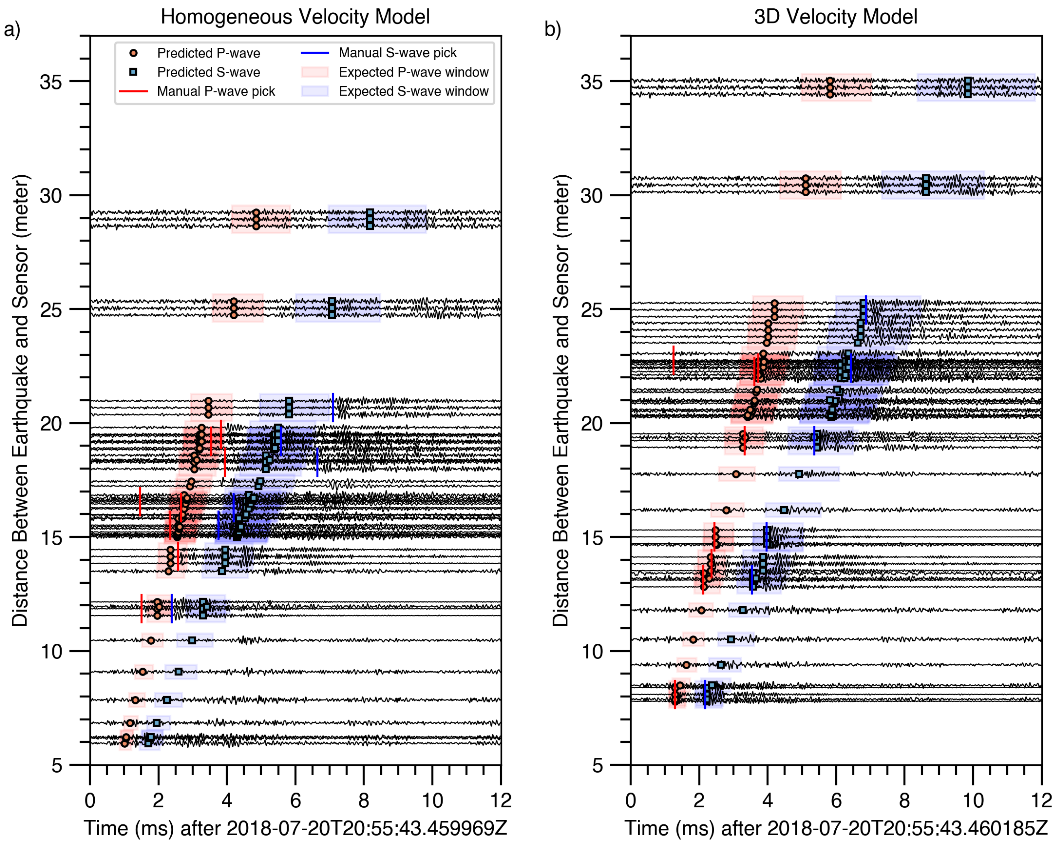

Figure 12. A comparison of data fit between the homogeneous velocity model and the inverted 3D velocity model for a seismic event that occurred on July 20, 2018. The dots represent the predicted arrival times using (a) the homogeneous velocity model and (b) the final 3D model. Vertical bars indicate the measured phase arrivals. The shaded boxes indicate the expected time windows that were computed with a velocity range of 4.9-6.9 km/s for P-waves and 2.9-4.1 km/s for S-waves. This is an extreme example. For many seismic events, the improvements in data fits are not so dramatic.

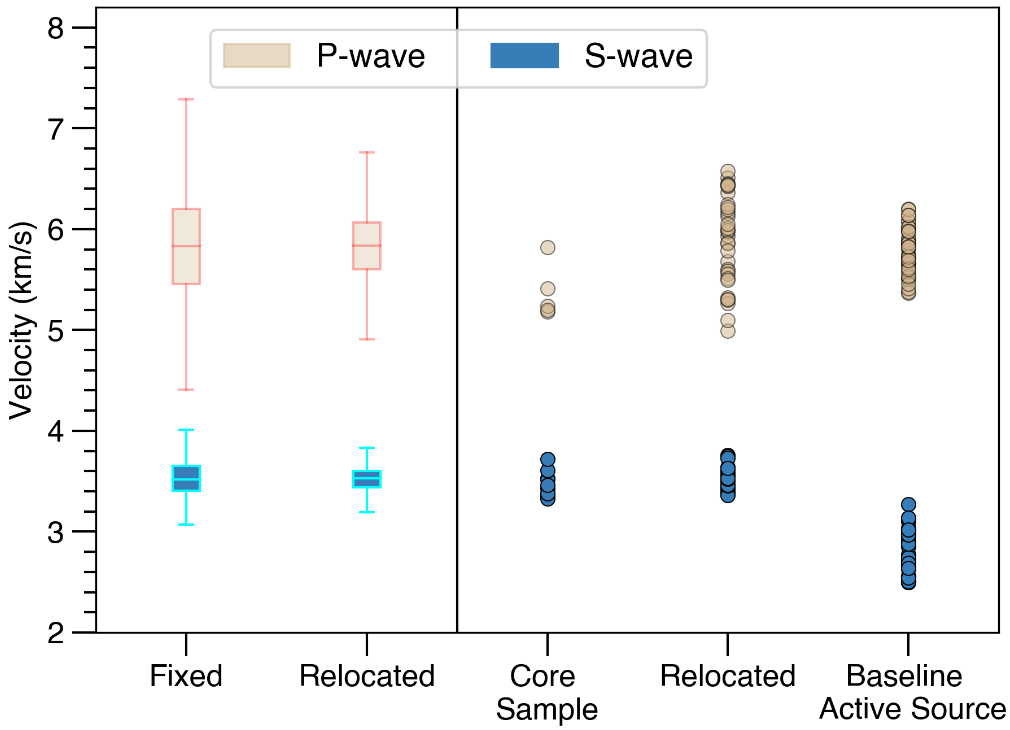

Figure 13. Absolute P-wave and S-wave velocity values for (left) the well-constrained volume (poorly constrained parts were excluded) and (right) near the core samples analyzed by Condon (2019). The location of the core samples is shown in Figure 1.

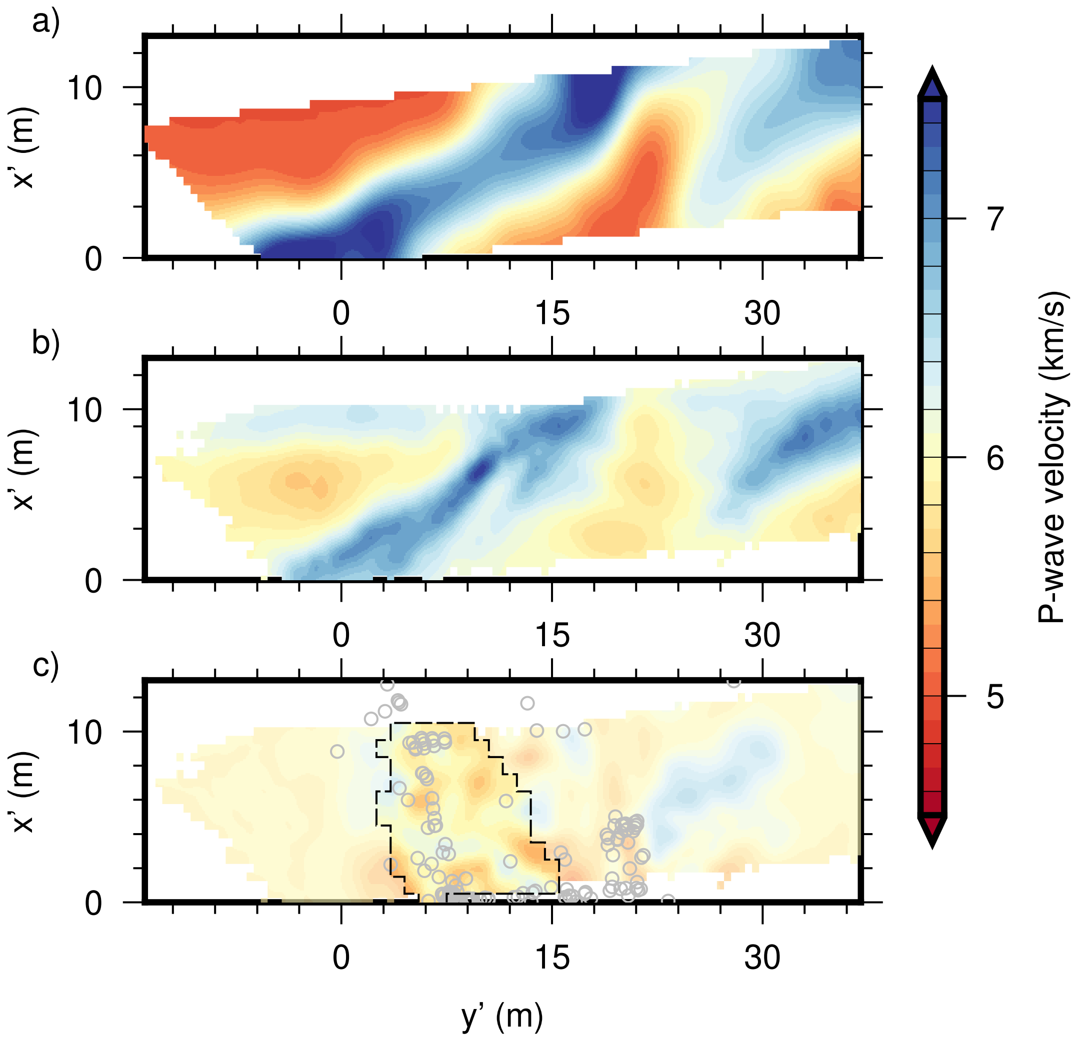

Figure 14. A comparison of P-wave velocity values on a plane obtained from a) a baseline model of an active seismic survey (Schwering et al., 2018), b) a reprocessed model of the active seismic survey, and c) the velocity model with seismic events relocated. The location of the plane is indicated in Figure 1. The open circles represent seismic events within 0.5 meter of the plane. The dimmed area is not well constrained due to lack of data coverage. The dashed lines denote the boundary of the dimmed area. For interpretation of the color in this figure, please see the online version.

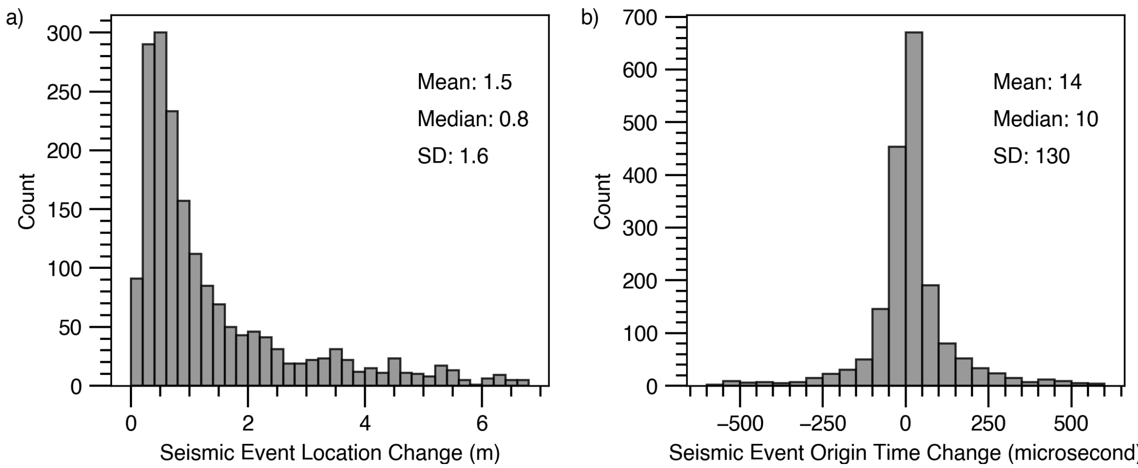

Figure 15. A histogram showing (a) the seismic event location changes and (b) origin time changes with respect to the original seismic event catalog. SD means standard derivation.

APPENDIX A: Members of the EGS Collab Team

EGS Collab Team includes J. Ajo-Franklin, T. Baumgartner, K. Beckers, D. Blankenship, A. Bonneville, L. Boyd, S. Brown, J.A. Burghardt, C. Chai, Y. Chen, B. Chi, K. Condon, P.J. Cook, D. Crandall, P.F. Dobson, T. Doe, C.A. Doughty, D. Elsworth, J. Feldman, Z. Feng, A. Foris, L.P. Frash, Z. Frone, P. Fu, K. Gao, A. Ghassemi, Y. Guglielmi, B. Haimson, A. Hawkins, J. Heise, C. Hopp, M. Horn, R.N. Horne, J. Horner, M. Hu, H. Huang, L. Huang, K.J. Im, M. Ingraham, E. Jafarov, R.S. Jayne, S.E. Johnson, T.C. Johnson, B. Johnston, K. Kim, D.K. King, T. Kneafsey, H. Knox, J. Knox, D. Kumar, M. Lee, K. Li, Z. Li, M. Maceira, P. Mackey, N. Makedonska, E. Mattson, M.W. McClure, J. McLennan, C. Medler, R.J. Mellors, E. Metcalfe, J. Moore, C.E. Morency, J.P. Morris, T. Myers, S. Nakagawa, G. Neupane, G. Newman, A. Nieto, C.M. Oldenburg, T. Paronish, R. Pawar, P. Petrov, B. Pietzyk, R. Podgorney, Y. Polsky, J. Pope, S. Porse, J.C. Primo, C. Reimers, B.Q. Roberts, M. Robertson, W. Roggenthen, J. Rutqvist, D. Rynders, M. Schoenball, P. Schwering, V. Sesetty, C.S. Sherman, A. Singh, M.M. Smith, H. Sone, E.L. Sonnenthal, F.A. Soom, P. Sprinkle, C.E. Strickland, J. Su, D. Templeton, J.N. Thomle, V.R. Tribaldos, C. Ulrich, N. Uzunlar, A. Vachaparampil, C.A. Valladao, W. Vandermeer, G. Vandine, D. Vardiman, V.R. Vermeul, J.L. Wagoner, H.F. Wang, J. Weers, N. Welch, J. White, M.D. White, P. Winterfeld, T. Wood, S. Workman, H. Wu, Y.S. Wu, E.C. Yildirim, Y. Zhang, Y.Q. Zhang, Q. Zhou, M.D. Zoback